Inorganic Chemistry

Article

pubs.acs.org/IC

# Photoluminescence Properties of Efficient Blue-Emitting Phosphor $\alpha$-$Ca_{1.65}Sr_{0.35}SiO_4$:$Ce^{3+}$: Color Tuning via the Substitutions of Si by Al/Ga/B

Kai Li,[†,‡] Mengmeng Shang,[†] Hongzhou Lian,*[,†] and Jun Lin*[,†]

[†]State Key Laboratory of Rare Earth Resource Utilization, Changchun Institute of Applied Chemistry, Chinese Academy of Sciences, Changchun 130022, P. R. China

[‡]University of Chinese Academy of Sciences, Beijing 100049, P. R. China

Supporting Information

**ABSTRACT:** A series of $Ce^{3+}$-doped $\alpha$-$Ca_{1.65}Sr_{0.35}SiO_4$ (CSSO) phosphors without and with the substitutions of Si by Al/Ga/B were synthesized via the high-temperature solid-state reaction process. X-ray diffraction patterns and Rietveld refinements were used to demonstrate the successful incorporations of Al/Ga/B into CSSO:$Ce^{3+}$. Without Al/Ga/B, the $Ce^{3+}$ singly doped CSSO phosphors present intense blue emission, which correspond to the broad emission bands in visible region with the wavelength range from 360 to 580 nm upon 350 nm excitation. The optimal emission intensity occurs in CSSO:0.05$Ce^{3+}$ sample with the emission peak wavelength at 436 nm. With the introduction of Al/Ga/B into the CSSO:0.05$Ce^{3+}$, the emission peak shifts from 436 to 457/465/446 nm under 365 nm excitation, respectively. The red shift of $Ce^{3+}$ emission is attributed to the polyhedral distortion of the cations, resulting in the enhancement of crystal field spitting due to the variations of the adjacent $(Al/Ga/B,Si)O_4$ polyhedron. Moreover, the temperature-dependent photoluminescence was determined to be of light impact to CSSO:$Ce^{3+}$ with the introduction of Al/Ga/B. This research is useful for enriching the emission colors of $Ce^{3+}$-activated phosphors.

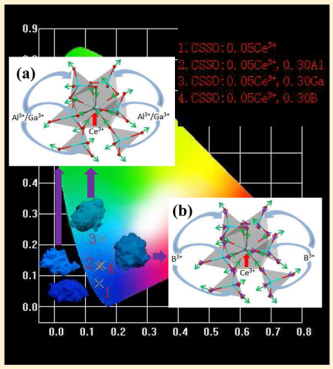


## 1. INTRODUCTION

Phosphor-converted white light-emitting diode (w-LED), which owns unique merits such as long durable lifetime, high efficiency, and low energy consumption, besides environmental friendliness, is regarded as a technology for next-generation solid-state lighting systems instead of current traditional fluorescent and incandescent lamps to face the global issues of environment pollution and energy consumption.[1] Combining blue-emitting InGaN LED chips with YAG:$Ce^{3+}$ to generate the white emission has been the common method in commercial application. However, the deficiency of red component leads to the issues of a poor color-rendering index and high correlated color temperature, which is commonly called cold white and is uncomfortable for our naked eyes after a long time. Therefore, employing the UV/near-UV LED chips with tricolor (blue, green, and red) phosphors has been considered to be another efficient and attractive way to realize the warm white light with high color uniformity and CRI, which would be anticipated as continuous investigation in near future.[2] Designing and searching novel efficient emission phosphors has been a hot topic in lighting field.[3] As we know, $Eu^{2+}$ and $Ce^{3+}$ can be good activators since their 4f−5d transitions are spin-allowed, whose 5d electronic shells are outside beyond 4f shells, resulting in the sensitivity to the crystal field and covalence. Therefore, they can generally present superior absorption bands in the spectral region of 250−450 nm, matching well with the UV and n-UV LED chips and broad emission spectra from blue to red region in $Eu^{2+}$/$Ce^{3+}$-doped phosphors. In this regard, $Eu^{2+}$/$Ce^{3+}$-doped phosphors have been still becoming the key component of investigation of the effectively activated and emitted phosphors. Additionally, the investigation on controllability of emission peaks of the tricolor phosphors also has been a hot issue to meet the requirement to obtain high-quality white light.

Silicate materials with many kinds of crystal structures have been studied as the hosts for doping rare earth elements to obtain various useful phosphors all the time based on many alluring characters such as mechanical, good thermal, chemical, and physical stabilities owing to their strong and severe frameworks with covalent Si−O bonds.[4] The silicate phosphors, represented by $Eu^{2+}$- or $Ce^{3+}$-doped orthosilicates $A_2SiO_4$ (A = Ca, Sr, Ba) and $M_{1-x}N_xSiO_4$ (M, N = Mg, Ca, Sr, Ba),[5] have attracted much attention due to their broad excitation/emission bands, tunable optical properties, and low costs. We notice that W. J. Park et al. have ever tried to synthesize the $Ca_{2-x}Sr_xSiO_4$:$Eu^{2+}$ phosphors with the variation of $x$, but the phases vary therein and are different from that of CSSO.[5h] Additionally, CSSO:$Eu^{2+}$ prepared by Sakthivel Gandhia et al. via solvothermal method presented two different phases;[5i] therefore, the photoluminescence (PL) properties were not sure to some extent. As far as we know, the PL properties of

**Received:** May 27, 2015
**Published:** August 6, 2015





DOI: 10.1021/acs.inorgchem.5b01197
*Inorg. Chem.* 2015, 54, 7992−8002

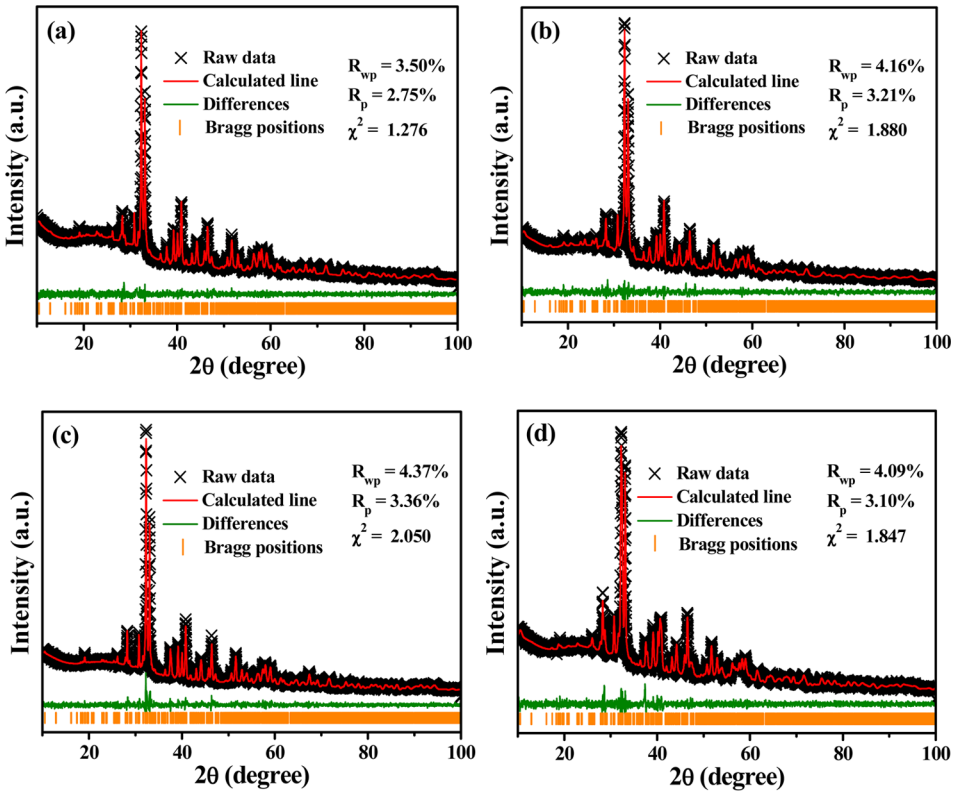


**Figure 1.** Rietveld refinements of powder XRD profiles of the representative CSSO:0.05$Ce^{3+}$ (a), CSSO:0.05$Ce^{3+}$, 0.20Al (b), CSSO:0.05$Ce^{3+}$, 0.20Ga (c) and CSSO:0.05$Ce^{3+}$, 20%B (d) samples.

pure $Ce^{3+}$-doped $\alpha$-$Ca_{1.65}Sr_{0.35}SiO_4$ phosphors have not ever been reported. Additionally, incorporation of Al into some phosphors to substitute Si can shift the emission to longer wavelength,[6] which can be effective to tune the emission band. However, the investigations of introductions of Ga and B, as the main group element of Al, into silicate phosphors are rare. Consequently, in this work the CSSO:$Ce^{3+}$ phosphors as well as $\alpha$-$Ca_{1.65}Sr_{0.35}Si_{1-x}(Al/Ga/B)_xO_4$:$Ce^{3+}$ were prepared by the solid-state high-temperature reaction method. The Rietveld refinements show that the pure CSSO phase phosphors were obtained. The crystal structure and luminescence properties of CSSO:$Ce^{3+}$ were also investigated. Without any substitution of Si by Al/Ga/B, the CSSO:$Ce^{3+}$ phosphors display intense blue emission under UV/n-UV excitation. Red shift of emission spectra can be found with the substitution of Si by Al/Ga/B, and the extent of red shift differs in each case, which is ascribed to the polyhedral distortion of cations occupied by $Ce^{3+}$, originating from the adjacent $(Si,Al/Ga/B)O_4$ tetrahedron.

## 2. EXPERIMENTAL SECTION

**2.1. Materials and Preparation.** The objective products with the stationary chemical composition of $\alpha$-$Ca_{1.65-x}Sr_{0.35}SiO_4$:$xCe^{3+}$ and $\alpha$-$Ca_{1.60}Sr_{0.35}Si_{1-m/n/l}(Al_m/Ga_n/B_l)O_4$:0.05$Ce^{3+}$ (abbreviated as CSSO:$xCe^{3+}$ and CSSO:0.05$Ce^{3+}$, $m$Al/$n$Ga/$l$B, $x$ = 0−0.15 and $m/n/l$ = 0.10−0.30 are the mole dopant concentration) were prepared by the high-temperature solid-state reaction route. The raw materials were $CaCO_3$ (analytical reagent (A.R.) grade), $SrCO_3$ (A.R.), $SiO_2$ (A.R.), $Al(OH)_3$(A.R.), $H_3BO_3$ (A.R.), $Ga_2O_3$ (99.99%), and $CeO_2$ (99.99%). Typically, the starting materials were weighed according to the given mole ratio and mixed with each other, then they were ground in an agate mortar with proper ethanol addition, after which the mixture was transferred to the crucible and transformed to the tube furnace and sintered at 1250 °C for 8 h under 20% $H_2$/80% $N_2$ atmosphere to gain the final samples. After that, the samples were furnace-cooled to room temperature with constantly reductive current and then polished once again into powders for the subsequent characterization.

**2.2. Measurement and Characterization.** All measurements were conducted using the finely ground powder. The phase structures of samples were analyzed by D8 Focus diffractometer at a scanning rate of 10° $min^{-1}$ in the 2$\theta$ range from 10° to 100° at the step of 0.02° and 2 s counting time per step with graphite-monochromatized Cu K$\alpha$ radiation ($\lambda$ = 0.154 05 nm). Powder diffraction data were calculated by the Rietveld method using the computer software GSAS package. Infrared spectra were collected on a VERTEX 70 Fourier transform infrared (FT-IR) spectrometer (Bruker). The Hitachi F-7000 spectrophotometer equipped with a 150 W xenon lamp as the excitation source was used to perform the PL measurements, and the diffuse reflectance spectra were measured using a Hitachi U-4100 spectrophotometer with the reflection of black felt (reflection 3%) and white $BaSO_4$ (reflection 100%), which was regarded as a reference standard. The luminescence decay lifetimes were acquired from a Lecroy Wave Runner 6100 Digital Osilloscope (1 GHz) using a tunable laser (pulse width = 4 ns, gate = 50 ns) as the excitation (Contimuum Sunlite OPO) source. PL quantum yields (QYs) of phosphors were obtained directly by the absolute PL QY measurement system (C9920−02, Hamamatsu Photonics K. K., Japan). All the above measurements were processed at room temperature (RT). Moreover, the temperature-dependent (298−523 K) PL spectra were recorded on a fluorescence spectrophotometer equipped with a 450 W xenon lamp as the excitation source (Edinburgh Instruments FLSP-920) with a temperature controller.

## 3. RESULTS AND DISCUSSION

Figure 1 demonstrates the Rietveld analyses of powder XRD profiles of the representative CSSO:0.05$Ce^{3+}$, CSSO:0.05$Ce^{3+}$, 0.20Al, CSSO:0.05$Ce^{3+}$, 0.20Ga, and CSSO:0.05$Ce^{3+}$, 0.20B samples conducted by the general structure analysis system (GSAS) method. The crosses, red lines, olive lines, and orange



DOI: 10.1021/acs.inorgchem.5b01197
Inorg. Chem. 2015, 54, 7992−8002

**Table 1. Detailed Crystallographic Data after Refinements of CSSO:0.05Ce$^{3+}$, CSSO:0.05Ce$^{3+}$, 0.20Al, CSSO:0.05Ce$^{3+}$, 0.20Ga, and CSSO:0.05Ce$^{3+}$, 0.20B Samples**

| sample | CSSO:0.05Ce$^{3+}$ | CSSO:0.05Ce$^{3+}$, 0.20Al | CSSO:0.05Ce$^{3+}$, 0.20Ga | CSSO:0.05Ce$^{3+}$, 0.20B |
|---|---|---|---|---|
| space group | *P*21*CN* | *P*21*CN* | *P*21*CN* | *P*21*CN* |
| symmetry | orthorhombic | orthorhombic | orthorhombic | orthorhombic |
| *a*, Å | 5.5516(2) | 5.5604(3) | 5.5572(1) | 5.5237(2) |
| *b*, Å | 9.3320(4) | 9.3386(4) | 9.3396(3) | 9.3276(3) |
| *c*, Å | 20.4957 (9) | 20.4944 (5) | 20.5161 (6) | 20.5787 (8) |
| *V*, Å$^3$ | 1061.83(9) | 1064.19(7) | 1064.84(7) | 1060.29(7) |
| Z | 12 | 12 | 12 | 12 |
| 2$\theta$ interval, deg | 10−100 | 10−100 | 10−100 | 10−100 |
| $R_{wp}$ | 3.50 | 4.16 | 4.37 | 4.09 |
| $R_p$ | 2.75 | 3.21 | 3.36 | 3.10 |
| $\chi^2$ | 1.276 | 1.880 | 2.050 | 1.847 |

bars represent experimental data, calculated values, differences between calculated and measured patterns, and Bragg positions, respectively. Crystal structure data of $\alpha$-$Ca_{1.65}Sr_{0.35}SiO_4$ (ICSD 39100) were used as the original modes to do the refinements. Crystallographic data and detailed refined parameters were listed in Figure 1 and Table 1, which show that the cell parameters *a*, *b*, and *c* do not change monotonously when B/Al/Ga substitute Si in CSSO:0.05Ce$^{3+}$, while the volume of cell monotonously increases with the increase of three-valence-electron atom radius. This result can be attributed to the integral effect of polyhedral distortion (including Si−O tetrahedron and Ca/Sr−O polyhedron) of cell lattice originating from the substitution of Si by B/Al/Ga elements. As depicted in Figure 1a−d, all the diffraction peaks can be assigned to the orthorhombic cell (*P*21*CN*) with parameters close to $\alpha$-$Ca_{1.65}Sr_{0.35}SiO_4$. The reliability factors of $R_{wp}$, $R_p$, and $\chi^2$ in Figure 1a−d indicate that the reflection conditions were well satisfied, and thereof pure CSSO phosphors were acquired with and without the substitutions of Si by B/Al/Ga component. X-ray diffraction (XRD) patterns of representative CSSO:0.05Ce$^{3+}$ and CSSO:0.05Ce$^{3+}$, *m*Al/*n*Ga/*l*B, *m*/*n*/*l* = 0.10 and 0.20 samples together with their enlarged parts between 31 to 35 degrees, as well as the standard reference of $\alpha$-$Ca_{1.65}Sr_{0.35}SiO_4$ (JCPDS 77−0399), are given in Figure 2. Main crystal orientations also were signed. Although some vacancies (point defects) in the oxygen lattice may be produced based on the charge balance because the $Al^{3+}/Ga^{3+}/B^{3+}$ are trivalent, while the $Si^{4+}$ is tetravalent, all the diffraction peaks are well-indexed to the reported $\alpha$-$Ca_{1.65}Sr_{0.35}SiO_4$ phase and no other distinct impurities can be observed in Figure 2a, indicating single-phase CSSO powders were obtained by the solid-state method, and the incorporation of Ce$^{3+}$ and Al/Ga/B did not arouse the significant change in structure within our experimental concentration range. By comparing the magnified peaks of representative samples between 31 and 35° in Figure 2b, we can find that the angle of diffraction shifts to higher value with the doping of B, contrary to lower ones as to Al and Ga, which can originate from the different atomic radii of Si (coordination number (CN) = 4, *r* = 0.26 Å) and B (CN = 4, *r* = 0.12 Å), Al (CN = 4, *r* = 0.39 Å), and Ga (CN = 4, *r* = 0.47 Å) and Al/Ga/B are successfully incorporated into the CSSO.

Figure 3a depicts the crystal structure of CSSO, which was reported by Udagawa, S. etal. in 1979.[7] Central Ca/Sr atoms form coordinated polyhedron with oxygen atoms, and Si−O tetrahedron can be independently formed, in which some oxygen atoms are bridge ones, while others are not. The Ca/Sr−O polyhedrons connect with Si−O tetrahedrons through

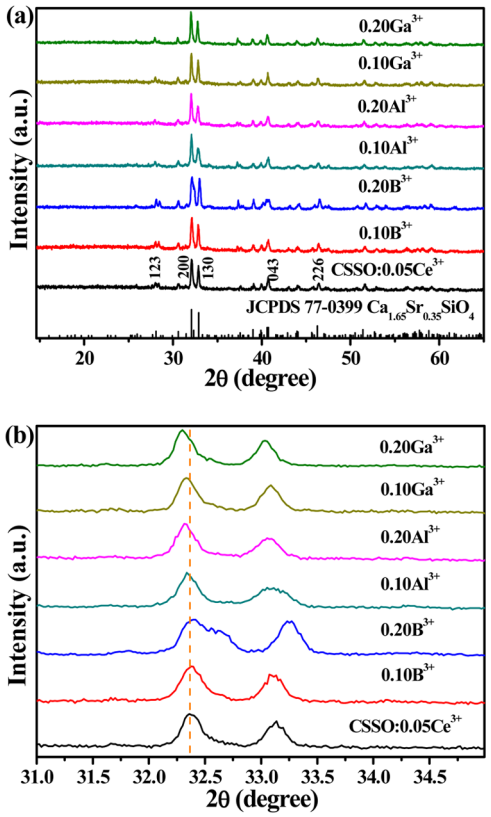


**Figure 2.** (a) XRD patterns of the representative CSSO:0.05Ce$^{3+}$ and CSSO:0.05Ce$^{3+}$, *m*Al/*n*Ga/*l*B, *m*/*n*/*l* = 0.10 and 0.20 samples, as well as the standard reference of $\alpha$-$Ca_{1.65}Sr_{0.35}SiO_4$ (JCPDS 77−0399). (b) The magnified patterns between 31 and 35° of CSSO:0.05Ce$^{3+}$, *m*Al/*n*Ga/*l*B, *m*/*n*/*l* = 0.10 and 0.20 samples.

one or two conjunct oxygen atoms between them. So, the distortion of Si−O tetrahedrons can result in the variation of Ca/Sr−O polyhedron. There are six kinds of Ca/Sr lattice sites, named Ca1/Sr1 to Ca6/Sr6 as presented in Figure 3b, with the corresponding coordination number of 5, 6, 4, 8, 7, and 7, respectively. We can easily accept that the volume of eight-coordinated Ca4/Sr4 polyhedron is bigger than others based on its biggest coordination number.

FT-IR spectrum was usually used to analyze the group information in the compound. One can find that the profiles of Ce$^{3+}$-doped CSSO with different doping concentration in Figure 4a and CSSO:0.05Ce$^{3+}$, 0.10Al/0.10Ga/0.10B, samples in Figure 4b are identical, which indicates that neither doping


DOI: 10.1021/acs.inorgchem.5b01197
*Inorg. Chem.* 2015, 54, 7992−8002

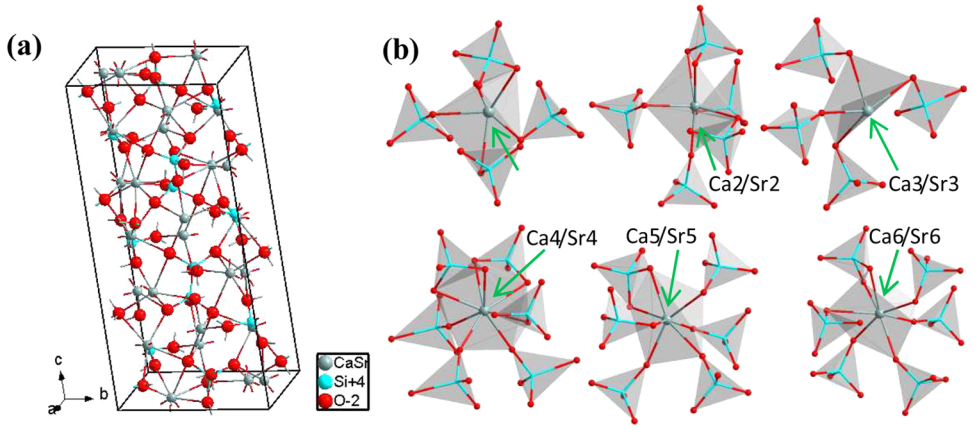


**Figure 3.** (a) Crystal structure of $\alpha$-$Ca_{1.65}Sr_{0.35}SiO_4$ compound. (b) Coordination environment of (Ca/Sr) atoms.

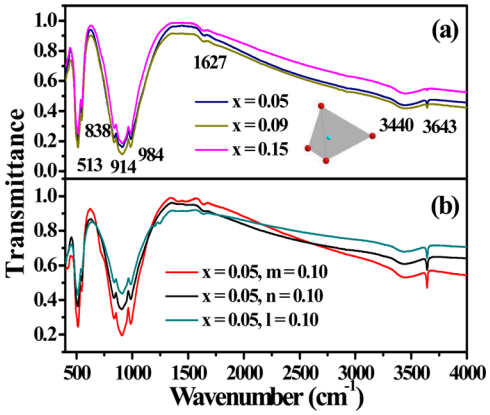


**Figure 4.** FT-IR spectra of the CSSO:$x$Ce$^{3+}$ ($x$ = 0.05, 0.09, and 0.15) (a) and CSSO:0.05Ce$^{3+}$, $m$Al/$n$Ga/$l$B, ($m/n/l$ = 0.10) (b) samples. (inset) The Si−O tetrahedron.

certain Al/Ga/B nor different concentrations of Ce$^{3+}$ in CSSO would transform the general structure of CSSO. The two vibration position around 513 cm$^{-1}$ corresponds to the bending mode in plane of Si−O−Si of the $SiO_4$ tetrahedron, and the group of peaks around 838, 914, and 984 cm$^{-1}$ are assigned to the asymmetric Si−O stretching modes of the $SiO_4$ tetrahedron, which are in accordance with the data [400−600 cm$^{-1}$ refers to $\delta(SiO_4)$, and 900−1100 cm$^{-1}$ refers to $\nu(SiO_4)$] reported in previous literature.[8] Another three obvious peaks of FT-IR spectra at ∼1627, 3440, and 3643 cm$^{-1}$ are assigned to the OH$^-$ stretching vibrations mode originating from the covered water on the surface of phosphors under air condition.

The diffuse reflectance spectra of undoped and Ce$^{3+}$-doped CSSO phosphors are displayed in Figure 5a. It is obvious that the profile of CSSO host is very different from those of the Ce$^{3+}$-doped CSSO ones. As for CSSO host, the band gap was approximately estimated to be ∼4.19 eV (297 nm, voilet short-dashed line). As Ce$^{3+}$ was doped into the CSSO host, many absorption bands ranging from 200 to 500 nm appear, corresponding to UV-green region, which are assigned to the Ce$^{3+}$ 4f$^1$−5d$^1$ transition. In addition, the absorption extent increases with continuously increasing Ce$^{3+}$ concentration in CSSO:$x$Ce$^{3+}$ phosphors, further demonstrating the absorption bands derive from the Ce$^{3+}$ ion. Figure 5b shows the reflectance spectra of CSSO:0.05Ce$^{3+}$ and CSSO:0.05Ce$^{3+}$, 0.10Al/0.10Ga/0.10B, which are similar to each other and therefore originate from Ce$^{3+}$ absorption transition.

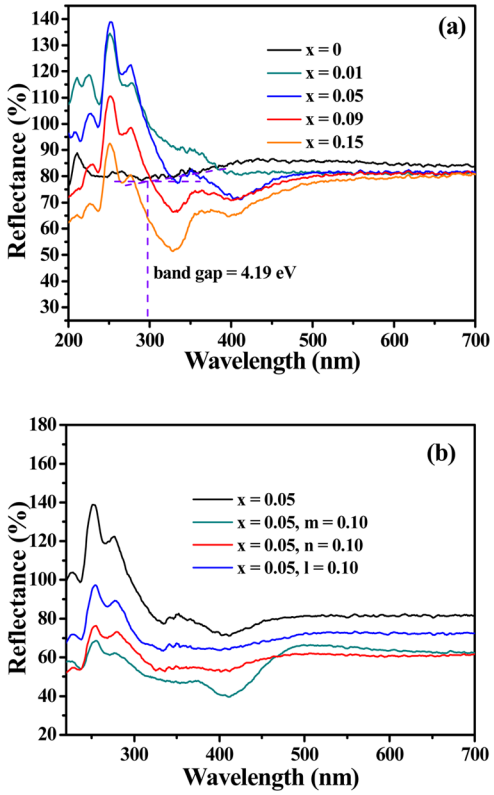


**Figure 5.** Diffuse reflection spectra of the CSSO:$x$Ce$^{3+}$ ($x$ = 0−0.15) (a) and CSSO:0.05Ce$^{3+}$, $m$Al/$n$Ga/$l$B, ($m/n/l$ = 0.10) (b) samples.

Figure 6a shows the PL excitation and emission spectra of CSSO:0.05Ce$^{3+}$ phosphor. Upon 350 nm excitation, the emission spectrum presents an asymmetric band extending from 360 to 600 nm centered at ∼436 nm, which is ascribed to the transition of 5d$^1$ to 4f$^1$ for Ce$^{3+}$. Moreover, the emission band can be decomposed into two symmetric bands centered at 427 (23 419 cm$^{-1}$) and 462 nm (21 645 cm$^{-1}$) by Gaussian deconvolution. The energy difference between them was calculated to be 1774 cm$^{-1}$, which is close to the energy gap of theoretical value of 2000 cm$^{-1}$ between the $^2F_{7/2}$ and $^2F_{5/2}$ states of Ce$^{3+}$.[9] On the basis of this, we can infer that Ce$^{3+}$ prefers to occupy only one kind of Ca/Sr crystallographic site, and the two bands analyzed above can account for the transitions from the lowest-lying excited state 5d$_z^2$ to the $^2F_{5/2}$ and $^2F_{7/2}$ ground states. It is accepted that the Ca4/Sr4 can be



DOI: 10.1021/acs.inorgchem.5b01197
Inorg. Chem. 2015, 54, 7992−8002

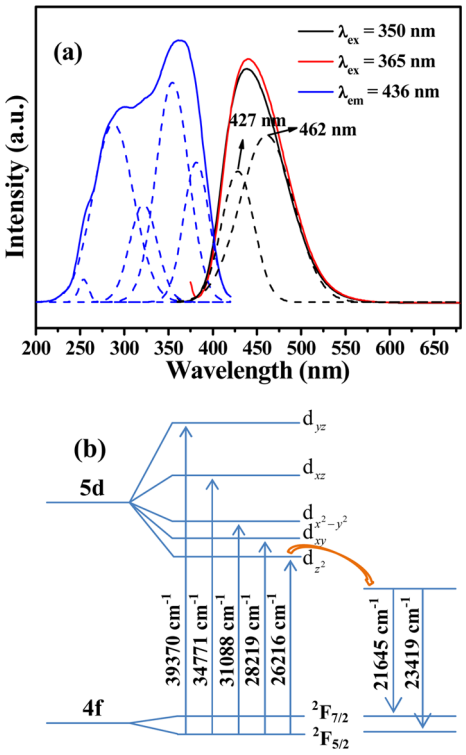


**Figure 6.** (a) PL excitation and emission spectra of CSSO:0.05Ce$^{3+}$ and (b) approximate energy-level scheme of Ce$^{3+}$ in CSSO host.

the most possible one because the Ca4/Sr4 has the eight coordinated-oxygen atoms around and the biggest volume of Ca4/Sr4−O8 polyhedron, as mentioned above, which make it easy to be replaced by other dopant atoms. However, to probe the energy structure of the Ce 5d and 4f levels in CSSO, the excitation ($\lambda_{em}$ = 436 nm) spectrum presents several peaks ranging from 200 to 450 nm with the maximum at 365 nm and are also analyzed by the peak deconvolution of Gaussian components. It can be deconvoluted into five peak components corresponding to excitations from $^2F_{5/2}$ state to five different levels of 5d orbitals, which are also consistent with the diffuse reflection spectra obtained in Figure 5a. Excitation from the $^2F_{7/2}$ state can be neglected because the spin−orbit splitting (1774 cm$^{-1}$ = 220 meV) is far larger than $k_BT$ (26 meV) at 300 K. The energy-level scheme for Ce$^{3+}$ in CSSO samples can be proposed and illustrated in Figure 6b on the basis of analyses of its excitation and emission spectra.

The variation of PL emission ($\lambda_{ex}$ = 365 nm) spectra of CSSO:$x$Ce$^{3+}$ with different concentrations ($x$ = 0.001, 0.005, 0.01, 0.03, 0.05, 0.07, 0.09, 0.12, and 0.15) of Ce$^{3+}$ and emission intensities together with emission peaks is displayed in Figure 7a,b, respectively. With increasing Ce$^{3+}$ concentration, the profiles of emission bands are identical with each other except for the emission intensity and peak positions. Moreover, the emission intensity increases monotonously until $x$ = 0.05, beyond which it begins to decrease in Figure 7a. This drop can be attributed to the general concentration quenching effect originating from the energy transfer among Ce$^{3+}$ ions.[10] Therefore, we can clearly see that the quenching concentration of Ce$^{3+}$ appears at $x$ = 0.05 from the PL intensities as a function

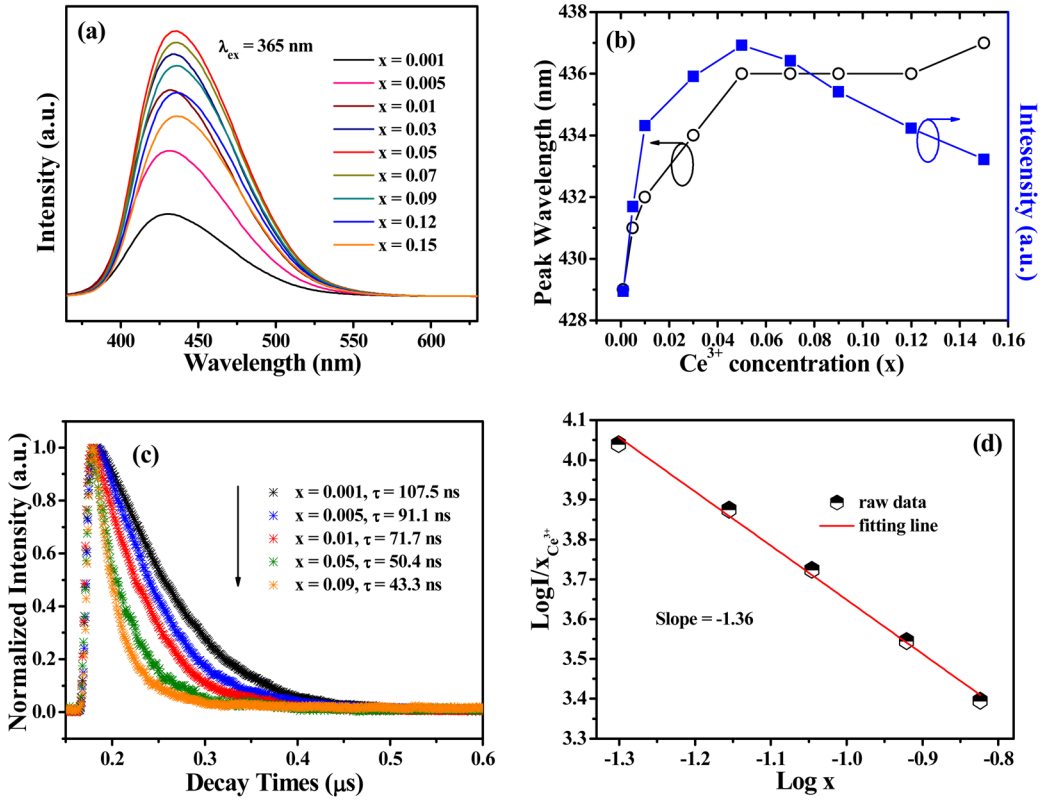


**Figure 7.** (a) PL emission spectra of CSSO:$x$Ce$^{3+}$ with different concentration of Ce$^{3+}$. (b) Variation of PL emission intensity and peaks wavelength as a function of Ce$^{3+}$ concentration in CSSO:$x$Ce$^{3+}$. (c) Decay curves of Ce$^{3+}$ emission (monitored at 436 nm and excited at 330 nm) in CSSO:$x$Ce$^{3+}$ samples. (d) Linear fitting of log($x$) vs log($I/x$) in various CSSO:$x$Ce$^{3+}$ phosphors beyond the concentration quenching ($x$ > 0.05).



DOI: 10.1021/acs.inorgchem.5b01197
Inorg. Chem. 2015, 54, 7992−8002

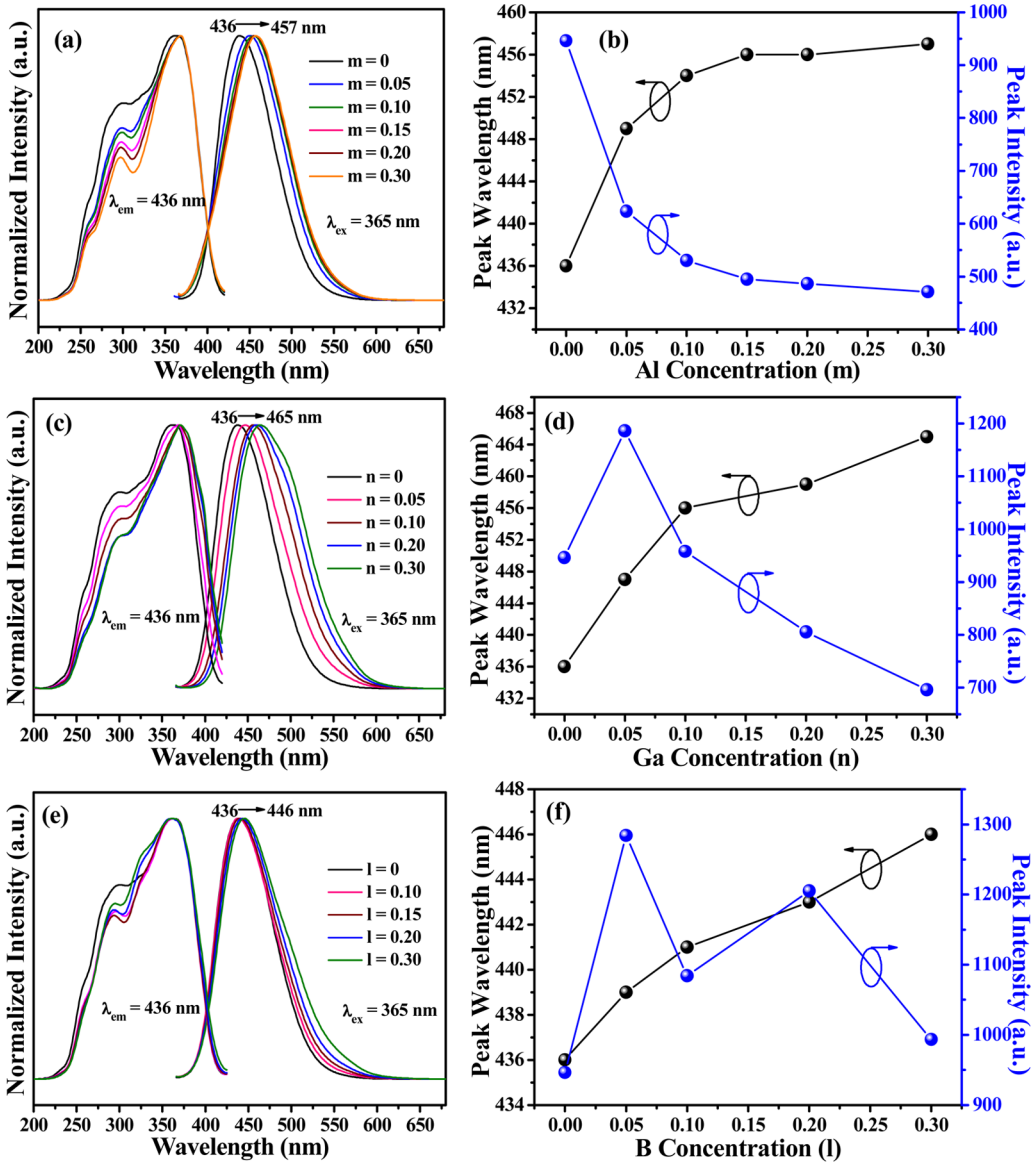


**Figure 8.** (a, c, e) The PL excitation and emission spectra of CSSO:0.05$Ce^{3+}$, *m*$Al^{3+}$, CSSO:0.05$Ce^{3+}$, *n*$Ga^{3+}$, and CSSO:0.05$Ce^{3+}$, *l*$B^{3+}$, respectively. (b, d, f) The corresponding variations of emission intensity and peak wavelength.

of $Ce^{3+}$ content (Figure 7b). Additionally, the emission peak shifts from 429 to 437 nm with increasing $Ce^{3+}$ content from $x$ = 0.001 to 0.15, which could originate from the variation of crystal field strength. As to this, the crystal field splitting ($D_q$) can be delivered as follows:[11]

$$D_q = \frac{1}{6} Ze^2 \frac{r^4}{R^5} \quad (1)$$

where $D_q$ is a measure of the energy level separation, $Z$ refers to the anion charge, $e$ is the electron charge, $r$ is the radius of the d wave function, and $R$ corresponds the bond length. When the $Ca^{2+}$ were occupied by the bigger $Ce^{3+}$ ions with eight coordination number, the distance between $Ce^{3+}$ and $O^{2-}$ became shorter, which resulting in the magnification of crystal field. Consequently, the lowest 5d band of $Ce^{3+}$ declined, and then finally led to the red shift of the emission wavelength with the increase of dopant $Ce^{3+}$ concentration. No other emission bands were observed in different $Ce^{3+}$-doped CSSO samples, which illustrates that $Ce^{3+}$ cannot occupy other five crystallographic sites although the $Ce^{3+}$ concentration increases in CSSO:$Ce^{3+}$ phosphors. We also measured the decay curves of $Ce^{3+}$ in different dopant concentration samples. The decay curves (monitored at 436 nm and excited at 330 nm) are plotted in Figure 7c, which deviate from exponential function and therefore can be approximately assessed by the simple equation copied below:[12]

$$\tau = \int_0^\infty I(t)\mathrm{d}t \quad (2)$$

where $\tau$ is the calculated lifetime value, and $I(t)$ refers to the normalized intensity of decay curves. According to the eq 2 and decay curves plotted in Figure 7c, the values of representative $Ce^{3+}$-doped samples are determined to be 107.5, 91.1, 71.7, 50.4, and 44.3 ns corresponding to $x$ = 0.001, 0.005, 0.01, 0.05, and 0.09, respectively. This indicates the monotonous decrease occurs with increasing $Ce^{3+}$ concentration in phosphors. Additionally, with the increasing of $Ce^{3+}$ content, the distance between $Ce^{3+}$ ions becomes shorter and shorter; thus, the probability of energy migration increases, which results in the


DOI: 10.1021/acs.inorgchem.5b01197
*Inorg. Chem.* 2015, 54, 7992−8002

Table 2. Emission Peak Positions with Different Concentration of Al/Ga/B Introduction in CSSO:0.05$Ce^{3+}$, *m*Al/*n*Ga/*l*B

| content (*m*/*n*/*l*) | | 0 | 0.05 | 0.10 | 0.15 | 0.20 | 0.30 |
|---|---|---|---|---|---|---|---|
| CSSO:0.05$Ce^{3+}$, *m*Al | emission peak (nm) | 436 | 449 | 453 | 456 | 456 | 457 |
| CSSO:0.05$Ce^{3+}$, *n*Ga | | 436 | 447 | 456 | | 459 | 465 |
| CSSO:0.05$Ce^{3+}$, *l*B | | 436 | | 439 | 441 | 443 | 446 |

decrease of emission intensity when the distance reaches small enough. Exchange interactions, radiation reabsorption, or multipole−multipole interactions may be responsible for the nonradiative energy transfer between different $Ce^{3+}$ ions. To determine which one occurs in $Ce^{3+}$-doped CSSO samples, the critical distance ($R_c$) between $Ce^{3+}$ ions should be given. The value of $R_c$ can be estimated with the following expression:[13]

$$R_c \approx 2\left[\frac{3V}{4\pi X_c N}\right]^{1/3} \quad (3)$$

where $V$ corresponds to the volume of the unit cell, $N$ is the available sites for the dopant in the unit cell in the unit cell, and $X_c$ is the critical concentration of dopant ions. For the $\alpha$-$Ca_{1.65}Sr_{0.35}SiO_4$ host, $N$ = 24, $V$ = 1071.03 Å$^3$, and $X_c$ is 5% for $Ce^{3+}$. As a consequence, the critical distance ($R_c$) was calculated to be ∼11.95 Å.

As mentioned above, the value of $R_c$ is much bigger than 5 Å, a distance for exchange interaction.[14] Therefore, the exchange interaction may have little possibility. The mechanism of radiation reabsorption is only effective when the fluorescence and absorption spectra are widely overlapping, which also does not intend to appear in this case. Consequently, we can conclude the electric multipolar interaction is most possible to be the energy transfer mechanism between $Ce^{3+}$ ions. The type of interaction between sensitizers or between a sensitizer and activator can be evaluated by the following equation:[15]

$$\frac{I}{x} = [1 + \beta(x)^{\theta/3}]^{-1} \quad (4)$$

where $I$ represents the emission intensity, $x$ is the activator ion concentration, which is beyond the quenching concentration of $x > 0.05$, $\beta$ is a constant for the fixed matrix under the same excitation conditions, and $\theta$ can represent the electric multipolar character, whose value = 6, 8, 10 corresponds to electric dipole−dipole, dipole−quadrupole, or quadrupole−quadrupole interactions, respectively. To obtain the concrete value of $\theta$, the curve of $\log(I/x)$ versus $\log(x)$ in CSSO:$Ce^{3+}$ phosphors beyond the quenching content of $Ce^{3+}$ is plotted in Figure 7d, which yields a straight line with a slope equal to $-1.36 = -\theta/3$ by linear fitting. Therefore, the value of $\theta$ is 4.08, approximately close to 6. This result indicates the dipole−dipole interaction dominates the energy transfer mechanism between $Ce^{3+}$ in CSSO:$Ce^{3+}$ phosphors for concentration quenching.

As reported previously, the effect of the structure and PL properties have been investigated with addition of Al in the $Sr_2Si_5N_8$:$Eu^{2+}$ phosphors.[16] However, the effect of PL emission and excitation spectra and structure with the addition of Al/Ga/B in CSSO:$Ce^{3+}$ have not been studied at all. Figure 8a,c,e shows the PL excitation ($\lambda_{em}$ = 436 nm) and emission ($\lambda_{ex}$ = 365 nm) spectra of CSSO:0.05$Ce^{3+}$, *m*Al (*m* = 0−0.30), CSSO:0.05$Ce^{3+}$, *n*Ga (*n* = 0−0.30), and CSSO:0.05$Ce^{3+}$, *l*B (*l* = 0−0.30), respectively, which present the profiles of them, are similar to that of CSSO:0.05$Ce^{3+}$, indicating the PL properties are originated from $Ce^{3+}$ ions. We can easily find that the PL excitation and emission peaks all shift to longer wavelengths with increasing dopant $Al^{3+}$/$Ga^{3+}$/$B^{3+}$ concentration. However, the extent of red shift of emission spectra are different from each other. For CSSO:0.05$Ce^{3+}$, Al, the emission peak shifts from 436 to 457 nm (21 nm red shift) under 365 excitation, as the increasing Al content from 0 to 0.30, which can be clearly observed in Figure 8b. We can also observe the variation of wavelength shift becomes placid after the Al content of 0.15. For CSSO:0.05$Ce^{3+}$, Ga, the emission peak can extend from 436 to 465 nm (29 nm red shift) when the doping concentration of Ga is 0.30 upon 365 nm excitation, as depicted in Figure 8d. When the B substitute Si in CSSO:0.05$Ce^{3+}$, the emission wavelength varies less than those of two above, it only shifts to 446 nm with the addition of B dopant content of 0.30, shown in Figure 8f. These detailed wavelengths with introduction of different content of Al/Ga/B in CSSO:0.05$Ce^{3+}$ are shown in Table 2. Moreover, the full width at half-maximum (fwhm) are all enlarged with the addition of Al/Ga/B. With the maximum addition of 0.30Al/0.30Ga/0.30B in CSSO:0.05$Ce^{3+}$ in this experiment, the value of fwhm is expanded from ∼75 to 82, 93, and 88 nm, respectively. In addition, by comparing the emission intensity of CSSO:0.05$Ce^{3+}$ with that of CSSO:0.05$Ce^{3+}$, *m*Al/*n*Ga/*l*B, we can find the effects of Al/Ga/B additions into CSSO:0.05$Ce^{3+}$ are also different from each other. With the increase of dopant Al content, the emission intensity of CSSO:0.05$Ce^{3+}$, Al decreases monotonously, while it increases first at Ga concentration of 0.05 and subsequently declines with further substitution of Si by Ga. However, the variation of intensity presents wave shape but generally declining with the increasing addition of B. Additionally, the decay curves of $Ce^{3+}$ in CSSO:0.05$Ce^{3+}$, *m*Al/*n*Ga (*m*, *n*, = 0, 0.10 and 0.30) were measured to study the dynamics of the luminescence, which show that the decay times increase lightly with the increases of doping concentrations of Al and Ga in CSSO:0.05$Ce^{3+}$, *m*Al/*n*Ga, as depicted in Figure 9a,b, respectively, while it is contrary

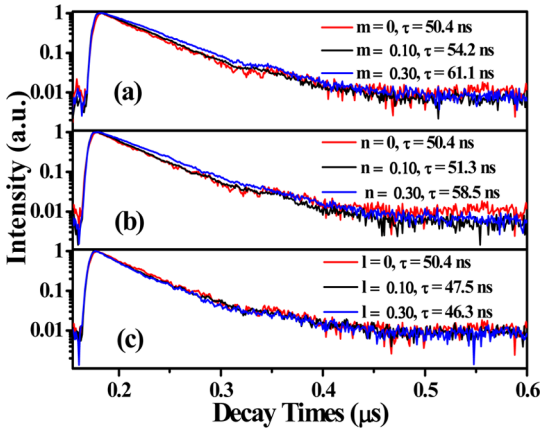


Figure 9. Decay curves of $Ce^{3+}$ emission band (monitored at 436 nm and excited at 330 nm) in CSSO:0.05$Ce^{3+}$, *m*Al (a), CSSO:0.05$Ce^{3+}$, *n*Ga (b), and CSSO:0.05$Ce^{3+}$, *l*B (c), respectively.



DOI: 10.1021/acs.inorgchem.5b01197
*Inorg. Chem.* 2015, 54, 7992−8002

to the one in CSSO:0.05Ce$^{3+}$, lB (l = 0, 0.10, and 0.30) samples according to eq 2 and curves in Figure 9c. However, the reason for this phenomenon is not easy to explain. We also measured the absolute quantum yields (QYs) of CSSO:0.05Ce$^{3+}$ and CSSO:0.05Ce$^{3+}$, 0.10Al/0.10Ga/0.10B, and CSSO:0.05Ce$^{3+}$, 0.30Al/0.30Ga/0.30B phosphors. The obtained values of absolute QYs are determined to be 33%, 50%/55%/60%, 54%/64%/70%, respectively. This illustrates that the QY increases with substitution of Si by Al/Ga/B at different extents, and this increase is not in agreement with their corresponding spectra. This phenomenon is attributed to the fact that the relationship between absolute quantum efficiency and luminescence is not closely relevant. The absolute quantum efficiency is related to the number of both absorption and emission photons. Therefore, although the luminescence of sample decreases with the Al substitutions, the absolute quantum efficiency can also be enhanced. It is accepted that the QY can be further optimized via the synthesis process and chemical composition in the future.

The crystal field splitting influenced by the polyhedron can be estimated by the $\varepsilon_{cfs}$ value.[17] A large $\varepsilon_{cfs}$ value is the primary reason for the large red shift of the first f−d transition, and there exists an empirical expression between the $\varepsilon_{cfs}$ value and the average distance ($R$) between the activator and the anions around:

$$\varepsilon_{cfs} = \beta_{poly}^{Q} R_{av}^{-2} \quad (5)$$

where $R_{av}$ is close to the average distance between the anions and cations substituted by Ce$^{3+}$, $\beta_{poly}$ refers to a constant that relies on the type of coordinating polyhedron and Q is 3 for Ce$^{3+}$. $\varepsilon_{cfs}$ is likely to decrease with the increase in coordination number and the average distance ($R$). Therefore, the crystal field splitting is primarily aroused by the average distance $R$ because the coordination number is eight for Ca4/Sr4 in CSSO:0.05Ce$^{3+}$, $m$Al/$n$Ga/$l$B. When different kinds of ions such as Al$^{3+}$ ($r$ = 0.39 Å), Ga$^{3+}$ ($r$ = 0.47 Å), and B$^{3+}$ ($r$ = 0.12 Å) here are introduced to substitute Si$^{4+}$ ($r$ = 0.26 Å) in CSSO:0.05Ce$^{3+}$, the Si−O tetrahedron can be regarded as Al/Si−O, Ga/Si−O, and B/Si−O tetrahedron, respectively; however, the phase structures are invariable (inferred from the XRD in Figure 2) and the emission peaks all produce red shift (seen from Figure 8), indicating the local structure should be changed. As depicted above in structure, since the dopant Ce$^{3+}$ will occupy the Ca4/Sr4 cation sites, the effective crystal structure of the investigated compound consists of disordered (Al/Si, Ga/Si, or B/Si)O$_4$ tetrahedron and Ca4/Sr4−O8 polyhedron. Distortion of the Al/Si, Ga/Si, or B/SiO$_4$ tetrahedron is linked to the increase in the average Al/Si or Ga/Si and decrease in the average B/Si ion sizes with increasing dopant concentration, respectively. Therefore, the Ca4/Sr4−O8 polyhedron connected with edges and bridge oxygen atom of Al/Si, Ga/Si, and B/SiO$_4$ distort with the increases of the average Al/Si and Ga/Si and decreasing B/Si ion sizes. The ionic radii of Al$^{3+}$ and Ga$^{3+}$ are bigger than that of Si$^{4+}$; thus, the Si−O tetrahedron is braced when Al$^{3+}$ or Ga$^{3+}$ is incorporated into Si−O tetrahedron around Ca4/Sr4. In addition, the positive charge of Al$^{3+}$ or Ga$^{3+}$ is less than that of Si$^{4+}$, so the attractive force between oxygen anions and Al$^{3+}$ or Ga$^{3+}$ is weaker than that of Si$^{4+}$. These two aspects result in the inflation of Si−O tetrahedron, contract and distort the Ca4/Sr4−O8 polyhedron, which arouses the decrease of average bond length of Ca4/Sr4−O8 polyhedron, as shown in Figure 10a. However, on one hand, the Si−O tetrahedron contracts based on the smaller ionic radius of B$^3$ than Si$^{4+}$ when B$^{3+}$ is introduced into Si−O tetrahedron; on the other hand, the attractive force between B$^{3+}$ and oxygen anions becomes weaker based on the less positive charge of B$^{3+}$ relative to Si$^{4+}$, inflating the volume, as depicted in Figure 10b. These two factors generally lead to the inflation of SiO$_4$ tetrahedron, resulting in the decrease of average bond length and distortion of Ca4/Sr4−O8 polyhedron. Therefore, the degree of decrease of bond length of Ca4/Sr4−O8 polyhedron increases with the sequence of B, Al, and Ga, which leads to the increases of crystal field splitting, according to eq 5 above, and to the shifted emission spectra in Figure 8. In addition, the variation of distorted degree of Ca4/Sr4−O8 polyhedron results in the different broadening of emission band in CSSO:0.05Ce$^{3+}$, $m$Al/$n$Ga/$l$B. The calculated CIE chromaticity coordinates are (0.146, 0.074) and (0.144, 0.131)/(0.154, 0.220)/(0.152, 0.136) for CSSO:0.05Ce$^{3+}$ and CSSO:0.05Ce$^{3+}$, 0.30Al/0.30Ga/0.30B, respectively, corresponding to the digital PL photos under 365 nm UV lamp radiation in Figure 10. The corresponding morphology of CSSO:0.05Ce$^{3+}$ and CSSO:0.05Ce$^{3+}$, 0.30Al/0.30Ga/0.30B phosphors were detected by scanning electron microscopy measurement. The sizes of particles are all approximately in the range from 5 to 20 $\mu$m, as depicted in Supporting Information (Figure S1), which is considered to be beneficial for LED fabrication.

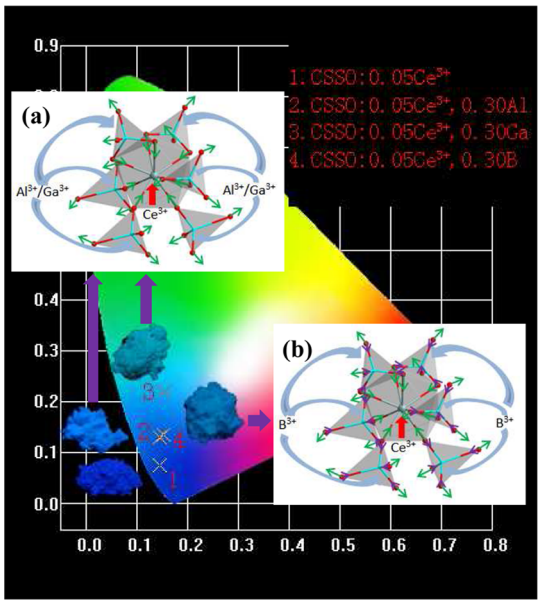


**Figure 10.** CIE chromaticity coordinates diagram and simple mechanism diagrams of substitutions of Si$^{4+}$ by Al$^{3+}$/Ga$^{3+}$ (a) and B$^{3+}$ (b) for Ca4/Sr4 site in CSSO:0.05Ce$^{3+}$.

The thermal stability of PL is one of the key parameters for the performance of phosphors applied in phosphor-converted LEDs. Therefore, the temperature dependence of the PL spectra (298−523 K) of CSSO:0.05Ce$^{3+}$ and CSSO:0.05-Ce$^{3+}$,0.30Al/0.30Ga/0.30B under 365 nm excitation is shown in Figure 11a−d. Results illustrate that the gradual decrease in emission intensities with increasing temperature can be ascribed to the thermal quenching effect via phonon interaction, in which the excited luminescence center is thermally activated through the crossing point between the excited and ground states. However, the emission peaks of all the emission


DOI: 10.1021/acs.inorgchem.5b01197
Inorg. Chem. 2015, 54, 7992−8002

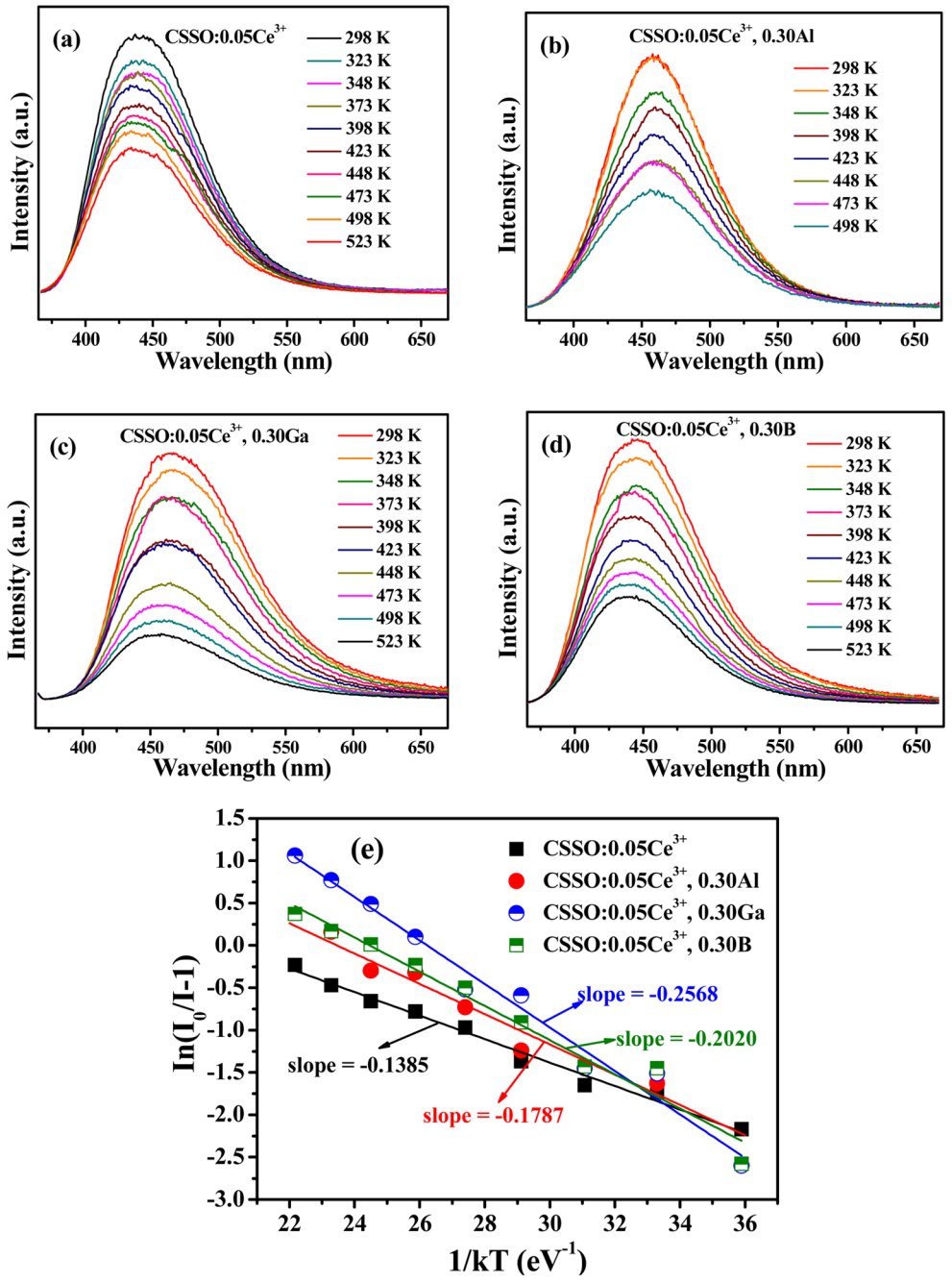


**Figure 11.** Temperature-dependent PL spectra of CSSO:0.05Ce$^{3+}$ (a), CSSO:0.05Ce$^{3+}$, 0.30Al (b), CSSO:0.05Ce$^{3+}$, 0.30Ga (c), and CSSO:0.05Ce$^{3+}$, 0.30B (d) phosphors under 365 nm excitation. (e) The relationships of $\ln(I_0/I - 1)$ vs $1/kT$ activation energy graph for thermal quenching for these samples.

components keep invariable. Since the phosphor should maintain operation at temperatures above 150 °C for a long period of time, the emission intensity at 150 °C relative to room temperature is important for us to assess its thermal stability. At 150 °C, the integrated intensity at 150 °C falls to ∼73% and 69%/63%/62% of their original values at room temperature for CSSO:0.05Ce$^{3+}$ and CSSO:0.05Ce$^{3+}$,0.30Al/0.30Ga/0.30B, respectively, which shows light decreases of thermal stability with the introductions of Al/Ga/B into CSSO:0.05Ce$^{3+}$. This may be attributed to the distortion of [$CeO_8$] and [$SiO_4$] polyhedral in crystal structure due to the different atomic radii between Al/Ga/B and Si. Additionally, the fwhm values of PL emission spectra of CSSO:0.05Ce$^{3+}$, CSSO:0.05Ce$^{3+}$, 0.30Al, CSSO:0.05Ce$^{3+}$, 0.30Ga, and CSSO:0.05Ce$^{3+}$, 0.30B increase from 75 to 85 nm, from 82 to 93 nm, from 93 to 102 nm, and from 88 to 97 nm corresponding to the temperature from 25 to 150 °C, respectively. This can be depicted by the Boltzmann distribution according to the following expression:[18]

$$\mathrm{fwhm}(T) = W_0\sqrt{\coth\left(\frac{hw}{2kT}\right)} \quad (6)$$

$$W_0 = \sqrt{8\ln(2)}\,(hw)\sqrt{S} \quad (7)$$



DOI: 10.1021/acs.inorgchem.5b01197
Inorg. Chem. 2015, 54, 7992−8002

where $W_0$ is the value of fwhm at 0 K, $hw$ is the energy of the lattice vibration that interacts with the electronic transitions, $S$ is the Huang−Rhys−Pekar parameter, and $k$ is the Boltzmann constant. It is assumed that $hw$ is the same for the $4f^1$ ground state and $5d^1$ excited state of $Ce^{3+}$ ions. As the temperature increases, the electron−phonon interaction gradually becomes dominant, and accordingly the fwhm of the emission line is widened. To evaluate the activation energy ($E_a$) for thermal quenching and further understand the thermal quenching phenomenon, the relationships of $\ln(I_0/I - 1)$ versus $1/kT$ activation energy graph for representative samples are plotted in Figure 11e according to the following expression raised by Arrhenius:[19]

$$\ln\left(\frac{I_0}{I}\right) = \ln A - \frac{E_a}{kT} \quad (8)$$

Herein, $I_0$ refers to the original emission intensity at room temperature 25 °C, $I$ is the emission intensity at different operating temperatures. $A$ represents a constant for an assigned host, $E_a$ is the activation energy of thermal quenching (which indicates the necessary energy to raise the electron from the relaxed excited energy level into the host lattice conduction band), and $k$ refers to the Boltzmann constant ($8.626 \times 10^{-5}$ eV). Thus, the $E_a$ were approximately determined to be 0.1358 eV and 0.1787/0.2568/0.2020 eV for CSSO:0.05$Ce^{3+}$ and CSSO:0.05$Ce^{3+}$, 0.30Al/0.30Ga/0.30B from the slopes of the fitting straight lines in Figure 11e, respectively. As for activation energy, a higher value means higher thermal stability. However, in this case, it is found that the activation energy data are not in agreement with the thermal quenching behavior of the substituted phosphors. It seems that the activation energies of some reported phosphors[20] also have big values of $E_a$, while their thermal quenching effects are worse than ours here. It may be because the activation energy data are approximate values obtained by fitting the raw data. In this process, it may produce some deviation, resulting in the mismatching.

## 4. CONCLUSIONS

A series of $Ce^{3+}$ singly doped CSSO phosphors without and with the substitutions of Si by Al/Ga/B have been synthesized via the high-temperature solid-state reaction process. XRD patterns and refinements of selected samples demonstrate their purity, which also can illustrate the successful incorporation of $Ce^{3+}/Al^{3+}/Ga^{3+}/B^{3+}$ into the CSSO host along with the diffuse reflection spectra. In $Ce^{3+}$ singly doped CSSO phosphors, the emission band can range from ∼360 to 580 nm upon 350 nm excitation. When Al/Ga/B is introduced into the CSSO:0.05$Ce^{3+}$, the red shift occurs in the emission peak of all samples. The crystal structure consists of six kinds of cation sites, in which the Ca4/Sr4 would be the most likely for $Ce^{3+}$ occupancy. The polyhedral distortion of the cations, which originates from the variation of adjacent $(Al/Ga/B,Si)O_4$ polyhedron, can contribute to the red shift of emission spectra. Moreover, the CSSO:$Ce^{3+}$ have good thermal stability, and the light impact to CSSO:$Ce^{3+}$ occurs with the introduction of Al/Ga/B. These results inspire us to search for new phosphors and explain the red shift of emission via the polyhedral distortion.

## ■ ASSOCIATED CONTENT

### Supporting Information

The Supporting Information is available free of charge on the ACS Publications website at DOI: 10.1021/acs.inorgchem.5b01197.

SEM images of representative phosphors CSSO:0.05$Ce^{3+}$, CSSO:0.05$Ce^{3+}$, 0.30Al, CSSO:0.05$Ce^{3+}$, 0.30Ga, and CSSO:0.05$Ce^{3+}$, 0.30B. (PDF)

## ■ AUTHOR INFORMATION


### Corresponding Authors

*E-mail: jlin@ciac.ac.cn.

*E-mail: hzlian@ciac.ac.cn.


### Notes

The authors declare no competing financial interest.

## ■ ACKNOWLEDGMENTS

This project is financially supported by the National Natural Science Foundation of China (NSFC Grant Nos. 51472234, 51172227, and 91433110), National Basic Research Program of China (Grant No. 2014CB643803), the Scientific and Technological Department of Jilin Province (Grant No. 20150520029JH), and Joint Funds of the National Natural Science Foundation of China (Grant No. U13012038).

## ■ REFERENCES


(1) (a) Park, S. H.; Lee, K. H.; Unithrattil, S.; Yoon, H. S.; Jang, H. G.; Im, W. B. *J. Phys. Chem. C* **2012**, *116*, 26850−26856. (b) Schmiechen, S.; Schneider, H.; Wagatha, P.; Hecht, C.; Schmidt, P. J.; Schnick, W. *Chem. Mater.* **2014**, *26*, 2712−2719. (c) Lee, S.-P.; Huang, C.-H.; Chen, T.-M. *J. Mater. Chem. C* **2014**, *2*, 8925−8931. (d) Kim, T.-G.; Kim, T.; Kim, J.; Kim, S.-J.; Im, S.-J. *J. Phys. Chem. C* **2014**, *118*, 12428−12435. (e) Hye Oh, J.; Yang, S. J.; Do, Y. R. *Light: Sci. Appl.* **2014**, *3*, e141. (f) Hao, J.; Cocivera, M. *Appl. Phys. Lett.* **2001**, *79*, 740−742. (g) Park, W. B.; Singh, S. P.; Yoon, C.; Sohn, K.-S. *J. Mater. Chem. C* **2013**, *1*, 1832−1839. (h) Tsang, M.-K.; Bai, G.; Hao, J. *Chem. Soc. Rev.* **2015**, *44*, 1585−1607.

(2) (a) Yang, X.; Tiam, T. S.; Yu, X.; Demir, H. V.; Sun, X. W. *ACS Appl. Mater. Interfaces* **2011**, *3*, 4431−4436. (b) Chen, J.; Liu, Y.; Fang, M.; Huang, Z. *Inorg. Chem.* **2014**, *53*, 11396−11403. (c) Gandhi, S.; Thandavan, K.; Kwon, B.-J.; Woo, H.-J.; Kim, C. H.; Yi, S. S.; Jeong, J. H.; Shin, D.-S.; Jang, K. *J. Mater. Chem. C* **2014**, *2*, 6630−6636. (d) Nakamura, S.; Fasol, G. *The Blue Laser Diode;* Springer: Berlin, Germany, 1996.

(3) (a) Chen, X.; Xia, Z.; Liu, Q. *Dalton Trans.* **2014**, *43*, 13370−13376. (b) Huang, C.-H.; Liu, W.-R.; Chan, T.-S.; Lai, Y.-T. *Dalton Trans.* **2014**, *43*, 7917−7923. (c) Huang, W.-Y.; Yoshimura, F.; Ueda, K.; Shimomura, Y.; Sheu, H.-S.; Chan, T.-S.; Chiang, C.-Y.; Zhou, W.; Liu, R.-S. *Chem. Mater.* **2014**, *26*, 2075−2085. (d) Medić, M. M.; Brik, M. G.; Dražić, G.; Antić, Ž. M.; Lojpur, V. M.; Dramićanin, M. D. *J. Phys. Chem. C* **2015**, *119*, 724−730. (f) Bai, G.; Tsang, M.-K.; Hao, J. *Adv. Opt. Mater.* **2015**, *3*, 431−462. (g) Zhang, Y.; Hao, J. *J. Mater. Chem. C* **2013**, *1*, 5607−5618.

(4) (a) Bandi, V. R.; Grandhe, B. K.; Jang, K.; Kim, S.-S.; Shin, D.-S.; Lee, Y.-I.; Lim, J.-M.; Song, T. *J. Lumin.* **2011**, *131*, 241−246. (b) Yuan, B.; Huang, Y.; Yu, Y. M.; Seo, H. J. *Ceram. Int.* **2012**, *38*, 2219−2223. (c) Wang, J.; Huang, Y.; Wang, X.; Qin, L.; Seo, H. J. *Mater. Res. Bull.* **2014**, *55*, 126−130. (d) Song, F.; Donghua, C.; Yuan, Y. *J. Alloys Compd.* **2008**, *458*, 564−568.

(5) (a) Guo, C.; Xu, Y.; Lv, F.; Ding, X. *J. Alloys Compd.* **2010**, *497*, L21−L24. (b) Lee, J. H.; Kim, Y. J. *Mater. Sci. Eng., B* **2008**, *146*, 99−102. (c) Pan, Z.; He, H.; Fu, R.; Agathopoulos, S.; Song, X. *J. Lumin.* **2009**, *129*, 1105−1108. (d) Choi, N.-S.; Park, K.-W.; Park, B.-W.; Zhang, X.-M.; Kim, J.-S.; Kung, P.; Kim, S. M. *J. Lumin.* **2010**, *130*,




DOI: 10.1021/acs.inorgchem.5b01197
*Inorg. Chem.* 2015, 54, 7992−8002

560−566. (e) Luo, Y. Y.; Jo, D. S.; Senthil, K.; Tezuka, S.; Kakihana, M.; Toda, K.; Masaki, T.; Yoon, D. H. *J. Solid State Chem.* **2012**, *189*, 68−72. (f) Barzowska, J.; Szczodrowski, K.; Krosnicki, M.; Kuklinski, B.; Grinberg, M. *Opt. Mater.* **2012**, *34*, 2095−2100. (g) Seong-Lee, J.; Kim, Y. J. *Ceram. Int.* **2013**, *39*, S555−S558. (h) Woo, H.-J.; Gandhi, S.; Kwon, B.-J.; Shin, D.-S.; Yi, S. S.; Jeong, J. H.; Jang, K. *Ceram. Int.* **2015**, *41*, 5547−5553. (i) Gandhi, S.; Thandavan, K.; Kwon, B.-J.; Woo, H.-J.; Jang, K.; Shin, D.-S. *Ceram. Int.* **2014**, *40*, 5245−5254. (j) He, H.; Fu, R.; Song, X.; Wang, D.; Chen, J. *J. Lumin.* **2008**, *128*, 489−493. (k) Liu, Y. W.; Fang, Q.; Ning, L. X.; Huang, Y. C.; Huang, S. Z.; Liang, H. B. *Opt. Mater.* **2015**, *44*, 67−72. (l) Kalaji, A.; Mikami, M.; Cheetham, A. K. *Chem. Mater.* **2014**, *26*, 3966−3975. (m) Fang, Y.; Li, L.; Chen, Y.; Wang, H.; Zeng, R. *J. Lumin.* **2013**, *144*, 13−17. (n) Jang, H. S.; Kim, H. Y.; Kim, Y.-S.; Lee, H. M.; Jeon, D. Y. *Opt. Express* **2012**, *20*, 2761−2771.

(6) (a) Wu, Q.; Wang, X.; Zhao, Z.; Wang, C.; Li, Y.; Mao, A.; Wang, Y. *J. Mater. Chem. C* **2014**, *2*, 7731−7738. (b) Miao, S.; Xia, Z.; Molokeev, M. S.; Chen, M.; Zhang, J.; Liu, Q. *J. Mater. Chem. C* **2015**, *3*, 4616−4622. (c) Won Jung, Y.; Lee, B.; Singh, S. P.; Sohn, K.-S. *Opt. Express* **2010**, *18*, 17805−17818. (d) Im, W. B.; Fellows, N. N.; DenBaars, S. P.; Seshadri, R. *J. Mater. Chem.* **2009**, *19*, 1325−1330.

(7) Udagawa, S.; Urabe, K.; Yano, T.; Takada, K.; Natsume, M. *Cem. Concr. Res.* **1979**, *33*, 35−38.

(8) (a) Buhler, G.; Zharkouskaya, A.; Feldmann, C. *Solid State Sci.* **2008**, *10*, 461−465. (b) Sunitha, D. V.; Nagabhushana, H.; Singh, F.; Sharma, S. C.; Dhananjaya, N.; Nagabhushana, B. M.; Chakradhar, R. P. S. *Spectrochim. Acta, Part A* **2012**, *90*, 18−21.

(9) (a) Zhou, J.; Xia, Z.; Yang, M.; Shen, K. *J. Mater. Chem.* **2012**, *22*, 21935−21941. (b) Geng, D.; Shang, M.; Zhang, Y.; Lian, H.; Cheng, Z.; Lin, J. *J. Mater. Chem. C* **2013**, *1*, 2345−2353. (c) Liu, W.-R.; Lin, C. C.; Chiu, Y.-C.; Yeh, Y.-T.; Jang, S.-M.; Liu, R.-S.; Cheng, B.-M. *Opt. Express* **2009**, *17*, 18103−18109. (d) Blasse, G.; Grabmaier, B. C. *Luminescent Materials;* Springer: Berlin, Germany, 1994; Chapter 3.

(10) Ju, H.; Wang, B.; Ma, Y.; Chen, S.; Wang, H.; Yang, S. *Ceram. Int.* **2014**, *40*, 11085−11088.

(11) (a) Que, M.; Ci, Z.; Wang, Y.; Zhu, G.; Xin, S.; Shi, Y.; Wang, Q. *CrystEngComm* **2013**, *15*, 6389−6394. (b) Rack, P. D.; Holloway, P. H. *Mater. Sci. Eng., R* **1998**, *21*, 171−219.

(12) (a) Guo, N.; Jia, Y.; Lü, W.; Lv, W.; Zhao, Q.; Jiao, M.; Shao, B.; You, H. *Dalton Trans.* **2013**, *42*, 5649−5654. (b) Li, K.; Geng, D.; Shang, M.; Zhang, Y.; Lian, H.; Lin, J. *J. Phys. Chem. C* **2014**, *118*, 11026−11034.

(13) (a) Blasse, G. *J. Solid State Chem.* **1986**, *62*, 207−211. (b) Blasse, G. *Philips Res. Rep.* **1969**, *24*, 131−144.

(14) (a) Dexter, D. L. *J. Chem. Phys.* **1953**, *21*, 836−850. (b) Liu, W. R.; Huang, C. H.; Wu, C. P.; Chiu, Y. C.; Yeh, Y. T.; Chen, T. M. *J. Mater. Chem.* **2011**, *21*, 6869−6874.

(15) (a) Van Uitert, L. G. *J. Electrochem. Soc.* **1967**, *114*, 1048−1053. (b) Van Uitert, L. G.; Johnson, L. F. *J. Chem. Phys.* **1966**, *44*, 3514−3521. (c) Xie, R. J.; Hirosaki, N. *Appl. Phys. Lett.* **2007**, *90*, 191101. (d) Li, K.; Shang, M.; Geng, D.; Lian, H.; Zhang, Y.; Fan, J.; Lin, J. *Inorg. Chem.* **2014**, *53*, 6743−6751.

(16) Chen, L. R.; Liu, H.; Zhuang, W. D.; Liu, Y. H.; Hu, Y. S.; Zhou, X. F.; Gao, W.; Ma, X. L. *CrystEngComm* **2015**, *17*, 3687−3694.

(17) (a) He, Y.; Zhang, J.; Zhou, W.; Han, J.; Qiu, Z.; Yu, L.; Rong, C.; Lian, S. *J. Am. Ceram. Soc.* **2014**, *97*, 1517−1522. (b) Zhang, J. L.; Zhang, W. L.; He, Y. A.; Zhou, W. L.; Yu, L. P.; Lian, S. X.; Li, Z. Q.; Gong, M. L. *Ceram. Int.* **2014**, *40*, 9831−9834.

(18) Dorenbos, P. *J. Lumin.* **2003**, *104*, 239−260.

(19) (a) Bhushan, S.; Chukichev, M. V. *J. Mater. Sci. Lett.* **1988**, *7*, 319−321. (b) Li, W. Y.; Xie, R. J.; Zhou, T. L.; Liu, L. H.; Zhu, Y. J. *Dalton Trans.* **2014**, *43*, 6132−6138.

(20) (a) Xia, Z.; Zhou, J.; Mao, Z. *J. Mater. Chem. C* **2013**, *1*, 5917. (b) Zhang, J.; He, Y.; Qiu, Z.; Zhang, W.; Zhou, W.; Yu, L.; Lian, S. *Dalton Trans.* **2014**, *43*, 18134.



DOI: 10.1021/acs.inorgchem.5b01197
*Inorg. Chem.* 2015, 54, 7992−8002